# A Coma Pattern-Based Autofocusing Method Resolves Bacterial Cold Shock Response at Single-Cell Level

SIHONG LI[1,4], ZHIXIN MA[1,2,4], YUE YU[1,4], JINJUAN WANG[1], YAXIN SHEN[1], XIAODONG CUI[3], XIONGFEI FU[1,2], AND SHUQIANG HUANG[1,2*]

[1]State Key Laboratory of Quantitative Synthetic Biology, Shenzhen Institute of Synthetic Biology, Shenzhen Institutes of Advanced Technology, Chinese Academy of Sciences, Shenzhen, 518055, China

[2]University of Chinese Academy of Sciences, Beijing, 100049, China

[3]Department of Physics, The University of Hong Kong, Hong Kong

[4]These authors contributed equally: Sihong LI, Zhixin MA, Yue YU.

*Corresponding authors: Shuqiang HUANG, shuqiang.huang@siat.ac.cn

***Abstract***

Imaging-based single-cell physiological profiling holds great potential for uncovering fundamental bacterial cold shock response (CSR) mechanisms, but its application is impeded by severe focus drift during rapid temperature downshifts required for CSR induction. Here, we introduce LUNA (Locking Under Nanoscale Accuracy), an innovative autofocusing method that leverages the coma pattern of detection light to characterize focus drift. LUNA improves the focusing precision down to 3 nm and extends the focusing range to at least 40 times the objective depth-of-focus. These advancements enable us to investigate the complete dynamics of bacterial single-cell CSR, revealing continuous cellular growth and division. We resolve a three-phase adaptation process characterized by distinct growth deceleration dynamics, and show that bacterial cells maintain robust size regulation and coordinate uniform adaptation to cold shock through synchronized growth and elapsed cycles. Notably, a model based on scattering theory reconciles the paradox between the growth lag of batch culture and continuous single-cell growth. These findings fundamentally transform our understanding of bacterial CSR and highlight LUNA's excellent potential for expanding state-of-the-art research in biology.

## 1. Introduction

The bacterial cold shock response (CSR) is a conserved adaptive mechanism triggered by abrupt temperature downshift[1]. It involves comprehensive physiological regulation that restores cellular growth homeostasis. Investigating CSR is essential for elucidating microbial survival mechanisms across clinical[2] and industrial settings[3]. This investigation advances fundamental understanding of stress adaptation principles and enables key translational applications, including novel antimicrobial development, enhanced biotechnological protein production, and improved cryopreservation protocols[4].

Over past decades, CSR has been extensively characterized at the population level[1]. Many bacterial species enter an acclimation phase immediately after cold shock, widely considered a growth arrest, as it is manifested by a constant optical density (OD)[5,6]. This phase is followed by the establishment of a new homeostasis exhibiting a reduced growth rate. While omics approaches have identified key CSR-associated proteins, their multilayered regulation and functional coordination remain poorly understood[1]. Many critical aspects of CSR, such as the physiological significance of the acclimation for bacterial cold adaptation and the specific cellular events occurring to the new homeostasis, remain underexplored. This is largely due to limitations inherent in population-level approaches.

Imaging-based single-cell physiological profiling, featuring high temporal resolution and throughput, has significantly advanced microbiology studies, enabling representative discoveries such as: identification of bacterial persister cell origins[7], propagation of molecular noise resulting in phenotypic heterogeneity[8], and validation of the bacterial "adder" behavior (wherein cells add a constant length extension between divisions)[9,10]. However, applying existing single-cell imaging methodologies for unbiased quantitative analysis of CSR faces significant challenges due to specific experimental requirements. Inducing CSR requires rapidly cooling the bacterial culture medium from 37 °C to below 15 °C within minutes. Standard temperature control systems in commercial microscopes lack such rapid cooling capacity. Crucially,

attempting this rapid cooling causes severe thermal drift, mechanically displacing the focal plane and resulting in irreversible focus loss.

As with general microscopy imaging workflows, acquiring statistically reliable data in single-cell CSR imaging requires maintaining precise focus across multiple fields of view over hours to days[11]. This necessitates an autofocus system to compensate for inevitable and unpredictable focus drift. A variety of strategies have been developed to this end over the years[12-19], and can be classified into two groups: imaging-based methods that capture image stacks along the optical axis and assess focus quality metrics to identify the in-focal plane through image analysis, reflection-based approaches that project auxiliary light to sense and measure the resulting reflection changes to directly gauge the distance between the objective and sample (Supplementary Note 1). Nevertheless, current implementations exhibit limited precision and range to accommodate stringent requirements of biological research, particularly the rapid large-span temperature shift required for CSR studies[20]. These limitations similarly hinder other advanced microscopy applications, for instance, imaging across large volume[14], single-molecule localization[21], and super-resolution imaging[16], etc. Meanwhile, computational extended depth-of-field techniques provide axial range extension through single-shot optical encoding or multi-focal fusion, circumventing repetitive autofocusing[22-24]. However, it remains fundamentally inadequate for CSR investigations due to incompatible high-resolution requirements and large drift exceeding its extended depth range.

Herein we propose LUNA (Locking Under Nanoscale Accuracy), a novel reflection-based autofocusing method that breaks through the limitations of the current solutions. LUNA is demonstrated to achieve exceptional focusing precision down to 3 nm while offering an ultra-large focusing range of at least 40 times the depth-of-focus (DOF) of the objective. With the help of LUNA, we investigated the bacterial CSR at the single-cell level by continuously monitoring thousands of individual *Escherichia coli* cells for more than ten hours. Multiple key aspects of bacterial CSR previously obscured in population-level measurements were resolved for the first time. Critically, *E. coli* cells continued to proliferate during

the acclimation. Our research revealed significant insights into detailed growth dynamics and facilitating growth mode transition, and further found that they resonate closely with prior molecular-level studies. Remarkably, *E. coli* exhibits a highly uniform, population-wide adaptation to cold shock without employing bet-hedging strategies[25]. These findings substantially advance our understanding of bacterial CSR and provide critical mechanistic insights. Furthermore, we analyzed our batch culture results on the basis of scattering theory, and concluded that the OD lag is actually the outcome of the synergy of changes in bacterial concentration and volume, which explains the controversies between single-cell and population observations.

## 2. Results

### 2.1. LUNA-based Platform for CSR Single-cell Physiological Profiling

Despite the observed population-level acclimation (growth arrest indicated by OD lag) immediately after cold shock[6], inherent cellular heterogeneity suggests diverse single-cell behaviors could underlie this net effect (Figure 1a). Several potential scenarios can be proposed: most cells abruptly halt growth simultaneously; some cells might undergo size reduction to adapt to growth-limiting low temperatures, similar to nutrient limitation[10,26]; or conversely, a less sensitive subpopulation may sustain growth, either maintaining or adjusting its growth rate, analogous to antibiotic-tolerant persisters[7] (Figure 1a). Importantly, these scenarios (individually or in combination) could collectively contribute to the OD lag. The actual dynamics are likely more complex when cell division and viability are also taken into account. Resolving these single-cell behaviors is essential, as it will elucidate the physiological basis of the acclimation and provide key insights into the molecular mechanisms of CSR[1].

To resolve these behaviors, we developed a bespoke LUNA-based platform for single-cell timelapse imaging under rapid temperature change (Methods, Figure 1b). This platform integrates a microfluidic-compatible temperature control device to rapidly and uniformly exert cold shock on individual cells. The microfluidic chip traps single cells in separate microchannels while maintaining steady growth via fresh medium flow[27], immersed in circulating distilled water for temperature maintenance and change. Precise and rapid cooling is accomplished by replacing the circulating water with ice-cooled water from the thermostatic bath, achieving performance unattainable with commercial air-based thermal controllers (Figure S1, Video S1). To overcome focal drift induced by thermal contraction during rapid temperature shifts, LUNA employs a displacement of coma pattern to monitor focal status and then provide continuous stabilization essential for reliable imaging (Video S2).

### 2.2. LUNA Optical Principle

In conventional reflection-based autofocusing methods, when an objective focuses the focus-aid light beam at the reflection interface, the intensity and contrast of the light spot are the highest. But they decrease

rapidly as the defocus distance increases, resulting in a constrained focusing range. Typically, it is also necessary to compensate for the offset distance between the desired focal plane and the reflection interface. However, the additional movement for the compensation leads to more fluctuations that could reduce the focusing accuracy[28]. To alleviate these limitations, for the first time to our knowledge, we introduce coma aberration in the diffraction pattern of the reflected auxiliary laser beam. This allows LUNA to lock onto the focal plan directly rather than introducing the offset, substantially improving focusing accuracy and range.

We investigated a thorough optical model for the propagation of an off-axis laser beam through an ideal lens in the presence of coma aberration[29] (Methods, Supplementary Note 2). This model gives an analytical expression of light distribution near the focus based on diffraction theory (Figure S2a). The presence of coma aberration causes the intensity distribution of the laser spot to concentrate on one side, forming a high-contrast crescent diffraction pattern (Figure 1c). The centroid locations (center of mass) of the brightest pattern along the z-axis exhibit a monotonic trend over a wide range away from the focal point (Figure 1d), suggesting that the defocus distance can be directly determined by the relative lateral displacement of the centroid location, which can be precisely measured. The contrast of the laser spot away from the focal plane is significantly enhanced compared to aberration-free system with the Airy pattern, thereby improving the accuracy of defocus detection and the focusing range (Figure S2b).

This model serves as a guide for the design and implementation of LUNA (Methods, Figure 1b). To validate and optimize the performance of LUNA, a numerical simulation of the optical setup was carried out based on ray tracing (Methods, Figure S3). The line projection of the crescent spot in the implementation conforms well with the simulation and shows supreme contrast. The simulation shows that LUNA has sufficient sensitivity (Figure 1e, the defocus distance $\Delta z$ can be magnified about 23 times at the detection plane). LUNA allows users to set the focal plane of interest by defining the centroid location on the detector as the origin without the need of setting any offset distance (Figure 1f, Figure S4). This

fundamentally decreases the intrinsic motive noises. Additionally, the wide focusing range allows a large tolerance for the offset. In the event of focus drift, a focusing procedure is initiated by repositioning the line spot to the origin through a feedback control.

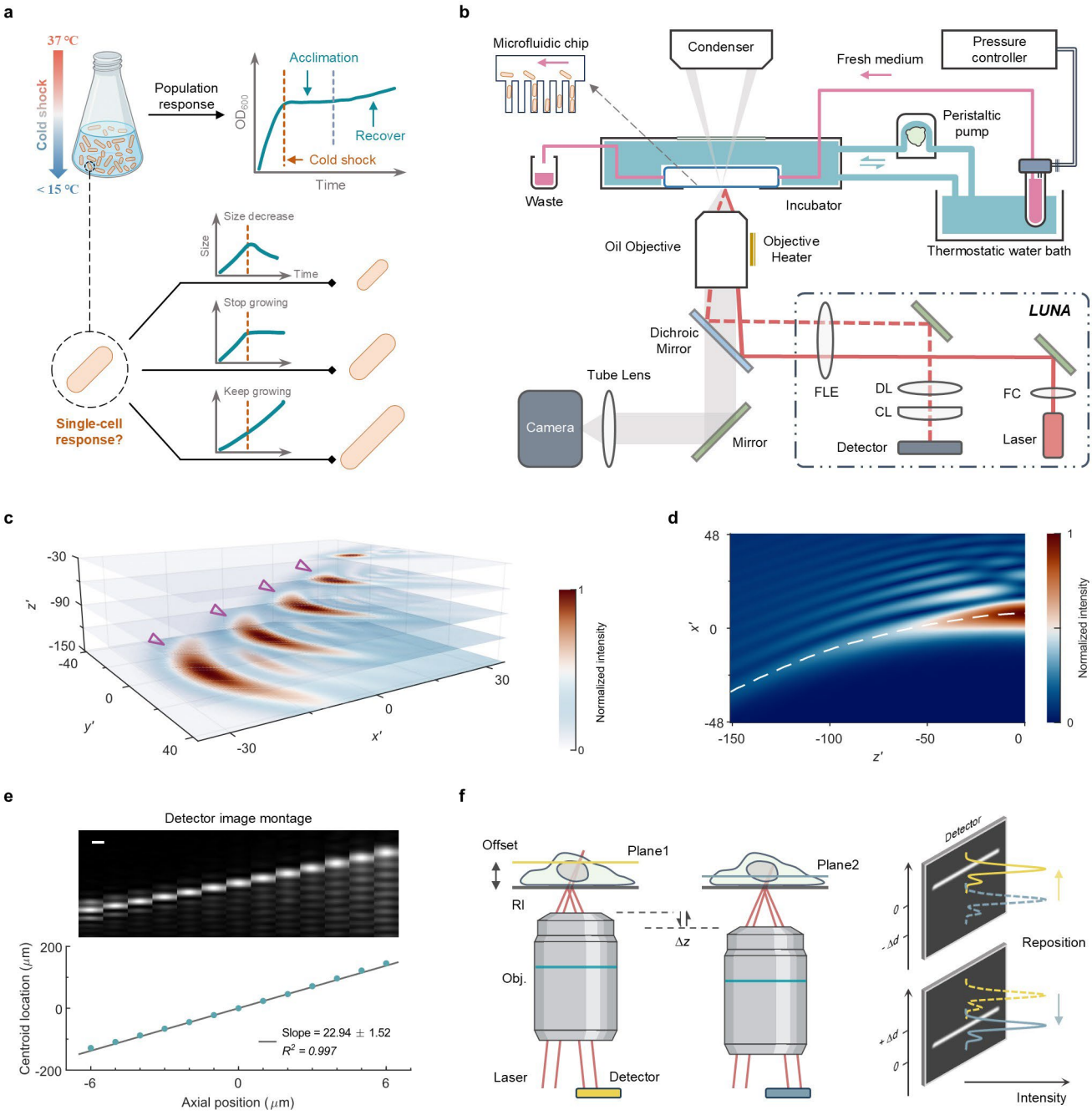


**Figure 1. LUNA-based platform for CSR single-cell imaging and illustration of optical principle. a**, Schematic of hypothesized single-cell bacterial CSR inferred from population-level OD analysis. The red dashed line indicates the time of cold shock (CS) application. After CS, OD ceases to increase, entering an

acclimation phase, after which it resumes increase. At the single-cell level, possible cellular size changes following CS include decrease, stasis, or continued increase. **b**, Schematic of our bespoke LUNA-based platform. Diagram includes the phase-contrast imaging unit, microfluidic-compatible temperature control device and LUNA optical path. Circulating water is indicated by the color cyan. In LUNA, laser beam is reflected into the main optical train by a dichroic mirror. Red dashed line: reflected light. FC, fiber collimator; CL, cylindrical lens; DL, detector lens; FLE, focal length extender. The implementation of LUNA follows this design. **c**, Computed intensity distribution in the dimensionless space under 100× objective. Computations were performed using the optical model: An off-axis Gaussian beam propagates through an objective lens of radius $a$ and focal length $f$. Coordinates ($x'$, $y'$, $z'$) equals ($k\beta x$, $k\beta y$, $k\beta^2 z$), where $k$ is wavenumber, $\beta = a / f$. Images at each axial position were individually normalized. Triangle markers indicate the crescent spots. **d**, Computed intensity distribution in x-z space. The dashed line indicates the centroid locations of the brightest crescent spots along the z-axis. Image contrast was adjusted for better exhibition (Gamma = 0.5). **e**, Magnified defocus distance on the detection plane in the ray tracing simulation. Linear regression with slope (95% confidence intervals) and fit goodness is shown. Scale bar, 60 μm. **f**, Working principle of LUNA. Set Plane1 (Plane2) as the interested focal plane by specifying the centroid location of the line spot on the detector as the origin. The defocus distance $\Delta z$ between the target and defocused Plane2 (Plane1) is inferred by the displacement $\Delta d$. Autofocusing is then achieved by repositioning the spot to the origin. RI, reflection interface; Obj., objective.

### 2.3. Performance Analysis of LUNA

The relationship between the measured centroid location and the physical axial position was calibrated (Methods, Figure S5a). LUNA shows an extensive focusing range and good linearity in a particular range (termed as linear range) around the focus, considerably exceeding the corresponding objective DOF. Within the linear range, the lateral displacement $\Delta d$ of the laser spot centroid is given by

$$\Delta d = A_M \cdot \Delta z \tag{1}$$

where $A_M$ represents the magnification coefficient. Despite some bias, this relationship can still be used to roughly estimate $\Delta z$ outside the linear range. The measurement repeatability was used to evaluate the degree of consistency during multiple tests. The results highlight the excellent ability of LUNA to accommodate large defocus distances (Table S1), thereby facilitating precise focusing across diverse spatial scales.

A drift threshold value was preset as a constraint criterion to determine the defocus status. LUNA effectively maintains the focal plane within a tight margin, while without compensation the focus drift can escalate to several microns within a dozen minutes (Figure 2a). Our results demonstrate that the focusing accuracy and precision (mean and standard deviation used)[30] remain small and consistent across different thresholds and objectives (Figure 2b, Figure S5b). Since the feedback autofocusing procedure results in an almost uniform distribution of errors, the measured precision closely approaches the theoretical value (threshold / √3). The best achievable precision is approximately 3 nm in our configuration (Table S1). Apart from the centroid displacement caused by focus drift, other perturbations affecting the precise localization of the centroid primarily arise from temporal fluctuations of the spot intensity. Numerical simulations were conducted to evaluate the effect of perturbations on the centroid location, which is limited to a few nanometers and can be ignored (Methods, Figure S7). Due to the small variance in focusing accuracy, the drift between successive autofocusing procedures is slight (Figure S8). This indicates that LUNA is suitable for common live or time-lapse imaging.

Short focusing time is another crucial feature of an autofocus system, especially for fast image acquisition. The focusing time was statistically tested under different procedure onset frequencies (Figure 2c, Figure S9). At lower frequencies, the focusing time exhibits a relatively significant variation across different thresholds. This variation can be attributed to an increase in the number of feedbacks needed to stabilize the focus, which arises from the larger axial drift presented. In practical applications, there is a tradeoff between pursuing better precision and shorter time consumption when determining the optimal threshold. Setting a sufficiently large threshold (i.e., greater than 15 nm, which is the optimal value in this

work) and a frequency above 10 Hz result in no considerable difference in focusing time under different conditions.

These advantages equip us to cope with drastic environmental perturbations during imaging, thereby facilitating the application of LUNA-based platform in bacterial CSR research. Upon initiation of cold shock (CS), the temperature within the sample incubator reached the target of 14 °C from 37 °C within 5 minutes (Figure 2d). This temperature shift caused significant relative drift between consecutive timepoints in the time-lapse imaging (maximum ~10 μm), much larger than the DOF (Figure 2d, Figure S10). LUNA effectively compensated for this drift, keeping the high-throughput imaging of approximately 1,100 cells simultaneously in focus (Video S2). The average focusing time at each location is around 0.6 seconds, enabling high temporal resolution imaging. (Figure 2d, 2e). Critically, no loss of focus occurred either at the moment of temperature downshift or during subsequent imaging (images in Figure 2e).

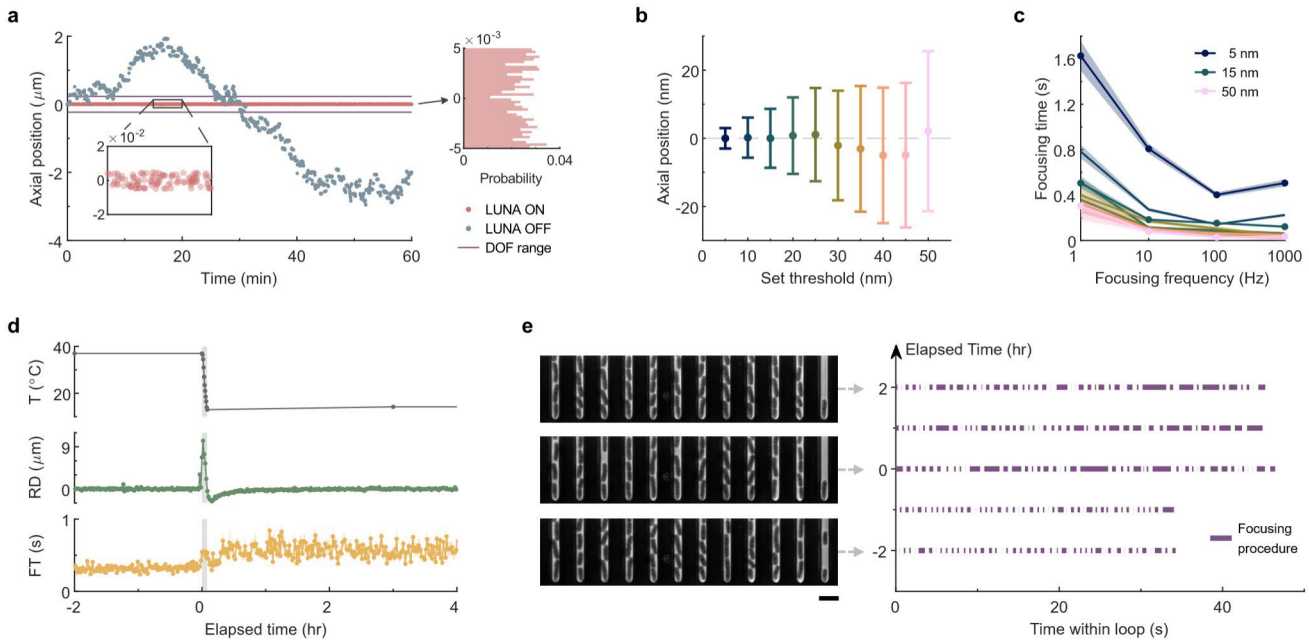


**Figure 2. Comprehensive performance metrics of LUNA. a**, Focus drift monitoring at 1 Hz in the laboratory environment. Right histogram shows the focal plane positions after each autofocusing procedure. **b**, Focusing accuracy and precision assessment. Dots and error bars represent the mean and s.d. values of the focus errors. Color palette in **b**, **c**, different set thresholds. **c**, Focusing time measurement for

autofocusing procedures at different intervals. Lines those marked with dots emphasize the representative constraints. **d**, System states over time when imaging bacteria. CS occurs at $t = 0$. T, temperature of cell environment; RD, relative drift of sample stage before autofocusing; FT, corresponding focusing time. Data in scatter form represent the average of all imaged sites ($n = 45$). Shaded region indicates the rapid temperature drop period. Error bands in **c**, **d**, s.e.m. **e**, Representative images and onset of autofocusing procedure. Scale bar, 4 μm. Intervals between consecutive procedures indicate the time consumption of phase-contrast imaging and stage motion.

### 2.4. Time-resolved Regulation of Growth Without Arrest Under CS

LUNA enables us to investigate the time-resolved behavior of bacterial CSR at the single-cell level. Cell morphological dynamics were extracted from time-lapse image sequences through a self-developed identification algorithm for subsequent statistical analysis (Methods, Supplementary Note 3). Single cells located at the bottom of each microchannel are inherited from one generation to the next after each cell division (Figure 3a). We distinguish the bacterial generations: the one encountering CS (G0), those before CS (GN), and those after CS (G1, G2, etc.). Upon application of CS, sustained division events are still maintained rather than stopping growth as generally believed based on the OD lag (Figure 3a, ~2 hours in our batch culture). Following acquisition of single-cell data, we addressed how growth and division are affected during CSR by analyzing the growth rate ($\lambda = dL / dt / L$, where $L$ is cell length). Cells exhibit no immediate growth arrest. Constant $\lambda$ before CS confirmed steady growth at 37 °C, while a stable but reduced $\lambda$ after 2 hours indicated a new steady growth at 14 °C (Figure 3b).

Analysis of growth deceleration ($d\lambda / dt$) revealed two inflection points at approximately 3- and 10-minute post CS (Figure 3c), delineating three adaptation phases. Phase I (to ~3 min) involves rapid cooling from 37 °C to 20 °C (Figure 2d), exhibiting drastic deceleration (approximately -6.25 $hr^{-2}$ on average). Surprisingly, the temperature dependence of $\lambda$ during this dynamic process also follows Arrhenius law observed at the population level in steady-state (Figure 3d), indicating growth deceleration is more likely

225 driven by temperature-dependent reaction kinetics rather than cellular regulated responses[31]. Despite
226 reaching 14 °C within 5 minutes, cells required ~2 hours to achieve the new steady growth, indicating
227 prolonged physiological adaptation after Phase I. Phase II (to ~10 min) shows immediate mitigation of
228 growth deceleration (approximately -2.97 $hr^{-2}$ on average), likely mediated by some constitutively
229 expressed cold shock proteins (CSPs, such as CspE) at 37 °C[32]. These CSPs are generally considered to
230 restore essential biochemical reactions during the acclimation[33]. Sustained elongation of already initiated
231 protein synthesis before CS[34.35] may also contribute. Phase III continues until the end of the acclimation
232 (to ~120 min), during which the temperature is kept constant at 14 °C. The further mitigated deceleration
233 (approximately -0.18 $hr^{-2}$ on average) suggesting more complex physiological regulation. Reanalysis of the
234 protein synthesis dynamics after CS revealed increase in CSPs synthesis (Figure 3e). These CSPs can
235 recover the protein translation more efficiently[36,37], likely contributing to the mitigation of growth
236 deceleration during Phase III. Following CS, ribosomes become underutilized as translation initiation is
237 significantly impaired at low temperature[5]. Although ribosome synthesis is reduced during this period, we
238 speculate that this reduction does not exacerbate the growth deceleration, as the dominant mitigating effect
239 is attributed to the upregulated CSPs. Towards the end of acclimation, a new balance between CSPs and
240 ribosomes is established, enabling establishment of new homeostasis (Figure 3b).

241 Growth mode analysis corroborated our physiological regulatory speculations in Phase III (Figure 3f,
242 3g). *E. coli* cells sustain exponential growth during steady-state[10], which is based on the view of
243 "autocatalytic loop" of biomass synthesis[38]. This means that a fixed portion of total newly synthesized
244 proteins is allocated to the ribosomes[39]. The progressive decline in new ribosome synthesis after CS
245 prevents the “autocatalytic loop”, manifested by immediate deviation from exponential growth (Figure 3e).
246 As the synthesis recovers in late phase III, a new homeostasis of “autocatalytic loop” in biomass synthesis
247 is achieved, i.e., the cell completes cold adaptation and resumes exponential growth.

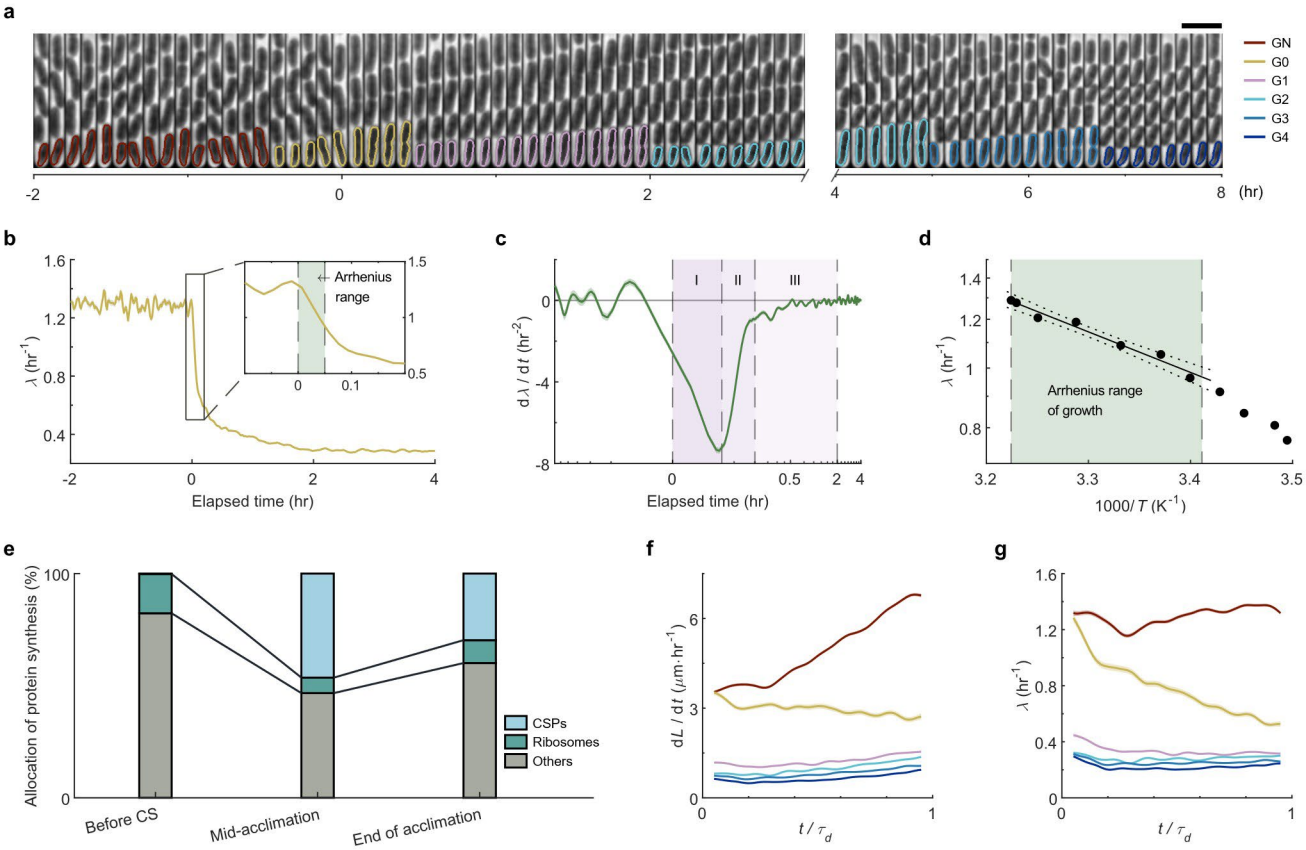


**Figure 3. Investigation of single-cell dynamics in CSR using LUNA. a**, Temporal montage of a single microchannel in the microfluidic chip. CS occurs at $t = 0$. Image was superimposed by cell contours with identified colors according to their generation marks. Timeline unit, hour. Intervals in the left and right panels are 6 and 10 mins, respectively. Scale bar, 4 μm. **b**, Average growth dynamics of cells. Arrhenius range of growth is shaded in inset. **c**, Growth deceleration as function of time. The time window of the three Phases is 0-3 min, 3-10 min and 10-120 min, respectively. Error bands in **b**, **c**, s.e.m. **d**, Temperature dependence of growth rate during the dynamic cooling process. Linear fitting to the reciprocal temperature and logarithm of $\lambda$ is shown as line. Dot lines indicate the 95% prediction bounds. Arrhenius range of growth is shaded. **e**, An illustration of the allocation of different proteins synthesis at different stage during CSR. Percentage data were retrieved from reference[5]. **f**, Average elongation rate across generations as function of normalized interdivision time. **g**, Average growth rate across generations as function of normalized interdivision time. Error bands in **f**, **g**, s.e.m. The color code in **f** and **g** marks the same generation as in **a**.

262 **2.5. Coordinated and Robust Single-cell Adaptation to CS**

263 The observed disruptions to exponential growth of individual cells suggest that the shock timing
264 within cell-cycle may be determinant; we therefore assessed whether the specific cell-cycle stage at the
265 time of shock influences subsequent heterogeneity and synchrony. To resolve sub-cell-cycle responses in
266 detail, we grouped cell lineages by the relative CS onset time since cell birth of G0, quantitatively defined
267 as $\xi$ (Figure 4a). This $\xi$-based grouping revealed the immediate transitions to linear growth in growth mode
268 (Figure S12), likely driven by CS-induced reprogramming of ribosome allocation (Figure 3e). Such
269 transitions may consequently perturb cell size homeostasis, prompting us to investigate its coordination
270 with size regulation mechanisms[40].

271 Bacterial cell size is a sensitive indicator of environmental stress[20,41-44]. We observed that they try to
272 maintain sufficient size (length) extensions in G0 as in the normal steady-state (Figure 4b, Table S2). The
273 division length ($L_d$) difference between G0 and its corresponding predecessor of each cell is small (median
274 of -1.3%). Furthermore, $L_d$ in G0 remains invariant across lineages with different $\xi$ (Figure 4c), consistent
275 with the ungrouped data. The cells then take an additional 3-4 generations for length stabilization to a
276 reduced value (Figure 4b). Besides, *E. coli* cells maintain a narrowly distributed size under the steady-state
277 as the "adder" behavior[9,10,45], which means length extension $\Delta L$ within a generation is independent of length
278 at birth $L_b$. Kendall's $\tau$ between rescaled $\Delta L$ and $L_b$ and the linear regression were examined, showing
279 almost no significant correlation (Figure 4d, $|\tau| \leq 0.1$ for all generations). The size distribution lacks distinct
280 subpopulations, and the standard deviation is almost constant across generations, indicating no substantial
281 increase in cell size variability (Figure 4d, Table S2). These data suggest that this "adder" behavior could
282 be maintained consistently during CSR, indicating that the intrinsic size regulation mechanisms continue
283 to function robustly, thus ensuring proper adaptation of cell size to the stress.

284 Further studies on cells with distinct $\xi$ and their progeny after CS revealed that cells exhibit highly
285 similar behaviors. The changes in $\lambda$ are highly synchronized in time, with the exact time lag between any

pair of $\xi$ not exceeding 2 min (Figure 4e, Figure S13). Alongside consistent size variation, *E. coli* exhibits no stress-specific subpopulations[7] (e.g., persisters), or CS-induced cell death (Video S3) indicating a sacrificial subpopulation[46]. This absence of bet-hedging strategies suggests that adaptation to CS is instead achieved through a collective and synchronized response. Surprisingly, the exact number of elapsed cycles at any moment since the CS event is also consistent across different cells (Figure 4f, 4g, Figure S14), implying the division timing is dependent of $\xi$. We verified the consistency of the elapsed cycle deviation over time. Compared with the steady-state, the deviation after CS does not increase significantly and is still within a small range (Figure S14). In other words, cells encountering a relatively late CSR will "accelerate" divisions to maintain synchronization.

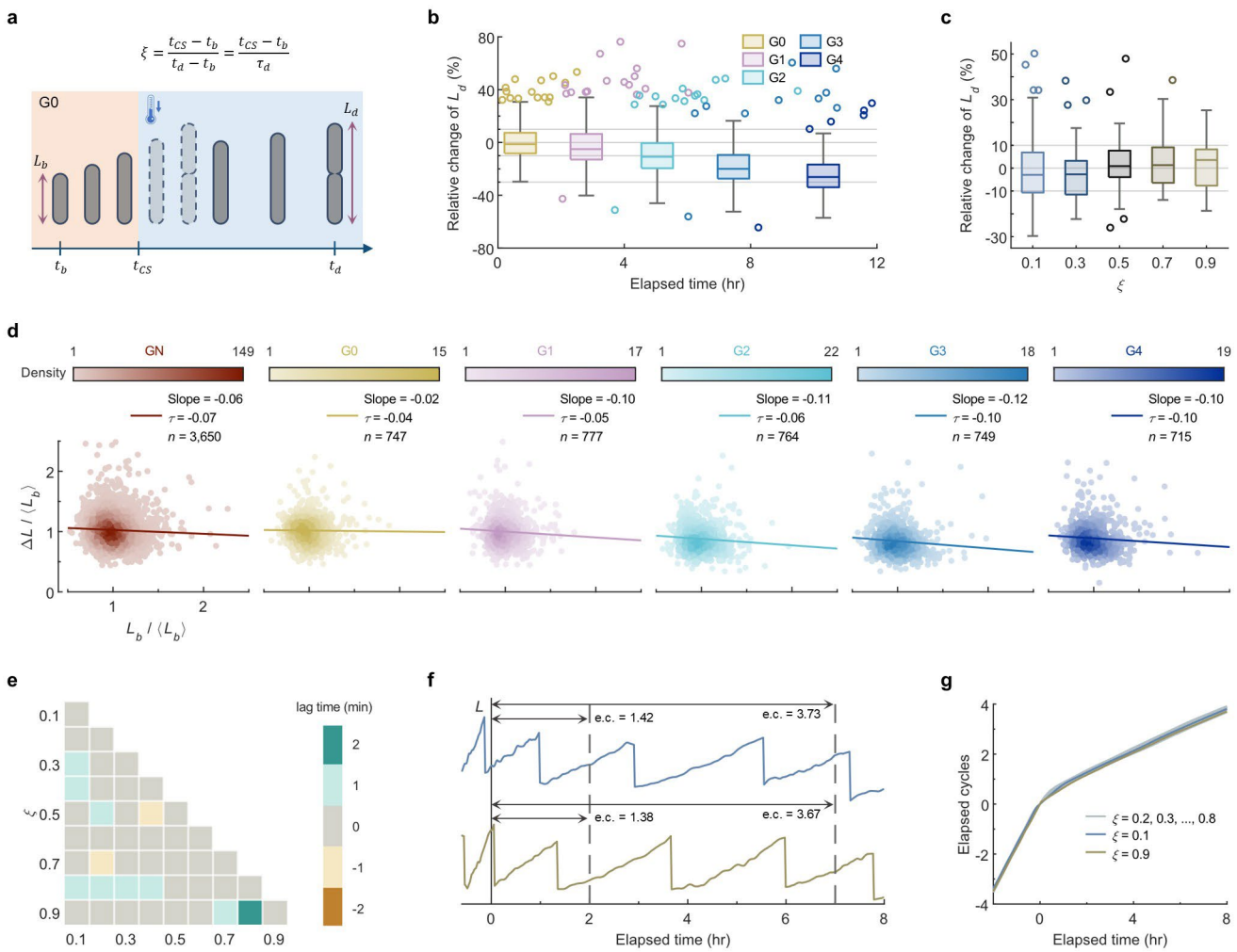


**Figure 4. Cell size regulation and growth synchronism under CS. a**, Notations in cell cycle. $\xi$, relative CS onset time since cell birth; $\tau_d$, interdivision time. Dashed cells, expected exponential growth in the

298 steady-state. **b**, Percentage change of division length of each generation after CS compares to GN. Data are
299 presented as box plots with the edges at the 0.25 and 0.75 quantiles, the central line at the median, and the
300 whiskers at the minima and maxima within 1.5× interquartile range from the box. Circles, outliers outside
301 the whiskers. Each box is located at the average division time of that generation. **c**, Percentage change of
302 division length of each group between G0 and their corresponding predecessors. Data are presented as box
303 plots as in **b**. **d**, Relationship between length extension and birth length across generations (rescaled by the
304 expectation of $L_b$). Gradient colors indicate data density of each generation. Linear regressions of all the
305 measured cycles and Kendall's $\tau$ are shown. $n$ represents cycle number. **e**, Lag matrix for distinct groups
306 of $\xi$. Values were computed by locating the cross-correlation maximum. **f**, Representative lineages with
307 synchronized elapsed cycles ($\xi$ is 0.10 and 0.90, respectively). e.c., elapsed cycles. **g**, Elapsed cycle
308 numbers of all lineages as functions of time. Errors shown in Figure S14b.

309 **2.6. Scattering Theory and Modeling Explanation of Proliferation Persistence During OD Lag**

310 The discoveries from single-cell experiments revealed that *E. coli* continues to proliferate after CS,
311 prompting us to reexamine batch culture experiments (Methods). In our results, the measured $OD_{600}$ curve
312 indeed showed an acclimation immediately following the rapid temperature downshifting (Figure 5a,
313 Figure S16a). Nevertheless, the cell concentration ($C$) continued to increase at a lower rate during the
314 acclimation. Meanwhile, the cell volume ($V$) decreases. Consistent with single-cell experiments, these
315 results confirmed that bacterial divisions do not cease after CS – contrary to conventional understanding.

316 Single-cell experiments show that CS doesn't cause significant cell death (Video S3). This means OD
317 lag is not a combined effect of partial cell lysis and partial growth. Therefore, a complex question is raised:
318 given that OD is a widely accepted indicator of total dry mass in experiments[47,48], why does the bacterium's
319 growth continue while the OD levels off? In theory, OD value involves not only the bacterial concentration,
320 but also light scattering by individual cells. Rayleigh scattering is the predominant scattering of light by
321 small particles compared to the wavelength of incident light. The Rayleigh-Gans approximation can

322 provide more accurate results if the interference scattered from different parts of the scatterer is taken into
323 account[49] (Methods, Supplementary Note 4, Figure S15). Numerical simulations were performed to
324 compute the total scattering cross section $\sigma$ of well-dispersed typical *E. coli* cells. The results show that $\sigma$
325 is not correlated to the aspect ratio (Pearson correlation coefficient -0.07) but is theoretically proportional
326 to $V^{1.34}$ (Figure 5b, Figure S15c). OD value is then given by $K\sigma C$, where $K$ is constant. A concise
327 dependency can be extracted as:

$$\mathrm{OD}_{600} = \alpha \rho_{dry}^{2} V^{1.34} C \tag{2}$$

328 where $\alpha$ is constant coefficient depending on the measurement conditions, $\rho_{dry}$ is the cellular dry-mass
329 density.

330 In the batch culture, $\sigma$ could be computed from the ratio of OD to $C$. It has a power relationship with
331 $V$, which agrees well with the theoretical relationship (Figure 5c, Figure S16b). This also indicates that $\rho_{dry}$
332 remains stable all the time even when cells experiencing CS[38] (a relative value for $\rho_{dry}$ is computed from
333 equation (2) by taking the square root of the ratio of the measured $\mathrm{OD}_{600}$ to the product of the measured $V$
334 $^{1.34}$ and $C$). Therefore, a theoretical OD curve can be deduced according to equation (2) (Figure 5a, Figure
335 S16a). The relationship holds when single scattering is applicable, which corresponds to the volume
336 concentration of scatterer is less than 0.001[50] (equivalent to $\mathrm{OD}_{600} < 0.5$ for *E. coli*). Batch culture studies
337 without CS verified that when $C$ is high, multiple scattering must be considered, and the cells become
338 physiologically different, leading to increased deviations (Figure S17)[26,51].

339 To further verify the validity of equation (2), total dry mass per ml ($M = \rho_{dry}VC$) as a function of
340 measured OD is also computed. In a steady-state, $M$ shows an excellent linear relationship with OD (Figure
341 5d, Figure S16c, 17b). When bacterial population reaches a new steady-state at a lower temperature, the
342 linear relationship can be well-fitted again. Some mass increment ($\Delta M$) during the acclimation indicates
343 population growth. In contrast, the corresponding OD may even decrease slightly due to the complicated
344 interplay (Figure 5e, Figure S18). A protein quantification measurement verified that total protein during
345 the acclimation still increased by about 13%, consistent with the trend and value of computed $\Delta M$

(Methods). Overall, these results suggest that OD is not an appropriate indicator of total dry mass under perturbed growing environment or unsteady growth, particularly for bacterial CS.

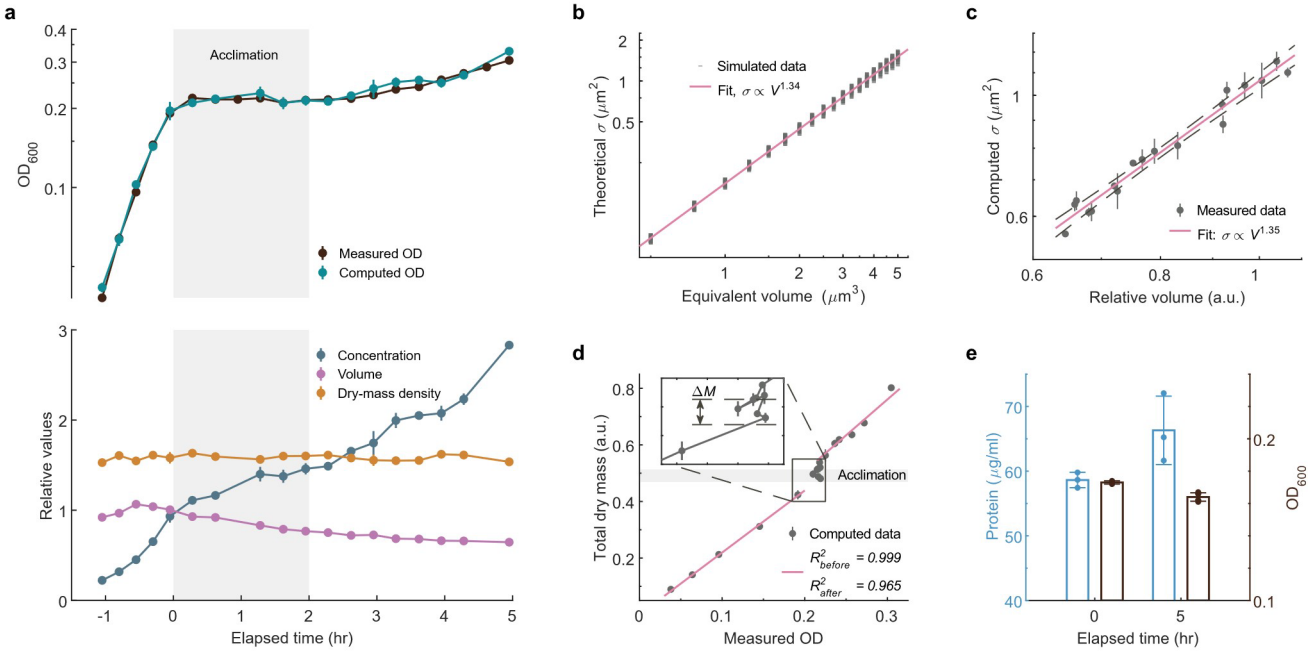


**Figure 5. Analysis of CS experiments of batch culture. a**, Measurements with temperature dropped to 14 °C. Measured and computed $OD_{600}$ values (top). Computed data was scaled at *t0*. Bottom: cell concentrations and average volumes extracted from the flow cytometer, normalized to *t0* and average value before CS, respectively. Relative cell density $\rho_{dry}$ was computed and scaled for present. Shaded region indicates the acclimation. **b**, Theoretical $\sigma$ across a range of equivalent cell volumes of simulated cells. Power exponent was determined by linear regression on the logarithmically transformed data ($R^2$ = 0.996, confidence interval is ±0.01). **c**, Computed $\sigma$ from experimental data as function of relative volume. Power exponent was obtained as same process in **b** ($R^2$ = 0.971, confidence interval is ±0.12). Dashed lines indicate the 95% prediction bounds. a.u., arbitrary units. **d**, Computed total dry mass plotted as a function of OD, together with linear fittings. Fitting for the acclimation has a $R^2$ of -0.263 (Pearson correlation coefficient -0.00). Mass increment during the acclimation is indicated as the height of the shaded area and marked in the inset. Error bars in **a**, **c, d**, s.d. **e**, Total protein measurement of MG1655 strain. Temperature drops to 12 °C were performed.

362 **3. Discussion**

363 Environmental stress profoundly influences bacterial physiology, population dynamics, and microbial
364 evolution. A key example is CS, a sudden temperature downshift known to induce growth arrest and
365 upregulate responsive genes in *E. coli*. High spatiotemporal imaging is the pivot for characterizing single-
366 cell physiological dynamics, where maintaining the focus precisely during environmental fluctuations
367 remains challenging (Video S1). Herein, we developed an integrated platform for uninterrupted high-
368 throughput time-lapse imaging of bacterial cells at 1-minute intervals. Under the instruction of an optical
369 model with coma aberration, we developed the LUNA method with nanoscale precision and ultra-large
370 focusing range, which can lock the focus directly and rapidly. Four representative objectives were tested
371 to evaluate LUNA's comprehensive performance metrics based on a range of criteria[52,53]. In our microscope,
372 the precision is limited by the accuracy of the servo motor used, which can be further improved by
373 employing piezoelectric motors with higher positioning accuracy to drive axial movement. The in-depth
374 time consumption analysis demonstrated the applicability of LUNA in tracking defocus variations either
375 in real-time or time-lapse imaging. Although the focusing time is sufficient for our experiments, it can be
376 reduced even further with faster motors and well-calibrated feedback control algorithms.

377 LUNA is successfully exploited in more extreme out-of-focus scenarios caused by severe temperature
378 fluctuations to study bacterial CSR at the single-cell level. The physiological profiling was performed and
379 revealed many characteristics of CSR that have been covered by population-level OD measurement. A
380 continuous three-phase growth decrement phenomenon in acclimation aligns with molecular-level
381 mechanisms, with cells sustaining both growth and division throughout. Each phase displayed a distinct
382 growth deceleration pattern: Phase I is primarily governed by Arrhenius law kinetics. Subsequently, CSR
383 is reflected in single-cell growth dynamics by the significant mitigation of the reduction in $\lambda$ when the
384 temperature drops below 20 °C (widely regarded as a triggering threshold of CSR, and marking Phase II
385 entry), with both Phase II and III explained by the dynamics of protein synthesis and the regulatory roles
386 of known CSPs. Effects related to ribosome allocation may also explain the transition to a linear growth

387 mode. Another noteworthy finding is that despite attenuated growth, bacterial cells maintain size
388 homeostasis and synchronize cell cycle progression, with no evidence of subpopulation formation or
389 reduced cellular viability. This homogeneous adaptive response suggests that *E. coli* employs a collective
390 stress-resistant strategy to tolerate transient temperature stress. Specifically, this strategy involves the
391 activation of a repertoire of pre-synthesized sensory and responsive molecules that persist in a standby
392 state[32,54] to counteract abrupt temperature fluctuations, thereby contributing to the ecological resilience and
393 community stability of bacterial populations[55]. In addition, our results show that OD is not an accurate
394 growth indicator in batch culture studies when the cell phenotype (size and division) is not maintained. We
395 summarized the OD value dependence and explained the paradoxical phenomenon of growth arrest
396 observed in population. Another scenario where OD may decrease occurs during nutrient downshift, in
397 which the bacteria size reduces[56].

398 From the perspective of evolution, it is reasonable for bacteria to keep growing and dividing after CS.
399 Individuals who can increase the population size during the acclimation can gain a competitive advantage
400 when entering a new steady-state. Based on the retention of some CSPs and nucleic acids at optimal growth
401 temperatures, it is foreseeable that bacteria may have developed the ability to sustain growth after CS long
402 time ago. Furthermore, such adaptive strategies can also cope with transient and periodic temperature
403 fluctuations, allowing cells to recover more swiftly to optimal growth following brief CS events without
404 the need to reboot their physiological activities. To further understand the mechanisms underneath those
405 phenomena, more physiological changes involving molecular mechanism exploration can be
406 investigated[57,58]. Looking forward, numerous questions regarding CSR remain unresolved. For instance,
407 why do distinct bacterial species employ divergent adaptive strategies during CSR[1]? How do bacterial cells
408 modulate their physiological states upon the reversion of temperature to optimal growth conditions?
409 Leveraging the LUNA-based platform, single-cell investigations hold the potential to provide critical
410 insights, facilitating a more systematic and rigorous exploration of these unresolved issues.

Beyond the instance in this work, LUNA offers excellent precision and can overcome the limitations of existing autofocusing solutions, thus enhancing many cutting-edge microscopy technologies, including super-resolution, single-molecule imaging, etc. Given its large focusing range, LUNA is capable of easily locking the focus in microscopy imaging across large volumes or at greater depths, such as multiphoton or light-sheet microscopy. The implementation of our method avoids complicated optics, alignment, and operation routines, posing its universal applicability to general microscopy techniques. As a result, we anticipate that LUNA will prevail in various research and industrial applications.

## References


1 Zhang, Y. & Gross, C. A. Cold Shock Response in Bacteria. *Annu. Rev. Genet.* **55**, 377-400 (2021).

2 Cardoza, E., Vira, D., Rao, A. & Singh, H. Altered gene expression of cold shock proteins under antibiotic exposure. J Antibiot 1–12 (2025).

3 Fang, S.-H., Chiang, S.-H., Hsu, S.-Y. & Chou, C.-C. Cold shock treatments affect the viability of Streptococcus thermophilus BCRC 14085 in various adverse conditions. Journal of Food and Drug Analysis 20, (2020).

4 Weber, M. H. W. & Marahiel, M. A. Bacterial Cold Shock Responses. *Science Progress* **86**, 9–75 (2003).

5 Zhang, Y. *et al.* A Stress Response that Monitors and Regulates mRNA Structure Is Central to Cold Shock Adaptation. *Mol. Cell* **70**, 274-286 (2018).

6 Jones, P. G., VanBogelen, R. A. & Neidhardt, F. C. Induction of proteins in response to low temperature in Escherichia coli. *J. Bacteriol.* **169**, 2092-2095 (1987).

7 Balaban, N. Q., Merrin, J., Chait, R., Kowalik, L. & Leibler, S. Bacterial Persistence as a Phenotypic Switch. *Science* **305**, 1622–1625 (2004).

8 Kiviet, D. J. *et al.* Stochasticity of metabolism and growth at the single-cell level. *Nature* **514**, 376–379 (2014).

9 Campos, M. *et al.* A Constant Size Extension Drives Bacterial Cell Size Homeostasis. *Cell* **159**, 1433-1446 (2014).

10 Taheri-Araghi, S. *et al.* Cell-Size Control and Homeostasis in Bacteria. *Curr. Biol.* **25**, 385-391 (2015).

11 Stephens, D. J. & Allan, V. J. Light microscopy techniques for live cell Imaging. *Science* **300**, 82-86 (2003).

12 Yazdanfar, S. *et al.* Simple and robust image-based autofocusing for digital microscopy. *Opt. Express* **16**, 8670-8677 (2008).

13 Ghaznavi, F., Evans, A., Madabhushi, A. & Feldman, M. Digital Imaging in Pathology: Whole-Slide Imaging and Beyond. *Annu. Rev. Pathol.: Pathol. Mech. Dis.* **8**, 331-359 (2013).

14 Silvestri, L. *et al.* Universal autofocus for quantitative volumetric microscopy of whole mouse brains. *Nat. Methods* **18**, 953-958 (2021).

15 Pinkard, H., Phillips, Z., Babakhani, A., Fletcher, D. A. & Waller, L. Deep learning for single-shot autofocus microscopy. *Optica* **6**, 794-797 (2019).

16 Wu, Y. C. *et al.* Three-dimensional virtual refocusing of fluorescence microscopy images using deep learning. *Nat. Methods* **16**, 1323-1331 (2019).

17 Li, S., Cui, X. & Huang, W. High resolution autofocus for spatial temporal biomedical research. *Rev. Sci. Instrum.* **84** (2013).

18 Zhang, X., Zeng, F., Li, Y. & Qiao, Y. Improvement in focusing accuracy of DNA sequencing microscope with multi-position laser differential confocal autofocus method. *Opt. Express* **26**, 895-904 (2018).

19 Bathe-Peters, M., Annibale, P. & Lohse, M. J. All-optical microscope autofocus based on an electrically tunable lens and a totally internally reflected IR laser. *Opt. Express* **26**, 2359-2368 (2018).

20 Knapp, B. D., Zhu, L. L. & Huang, K. C. SiCTeC: An inexpensive, easily assembled Peltier device for rapid temperature shifting during single-cell imaging. *PLoS Biol.* **18** (2020).

21 Beghin, A. *et al.* Localization-based super-resolution imaging meets high-content screening. *Nat. Methods* **14**, 1184-1190 (2017).

22 Dowski, E. R. & Cathey, W. T. Extended depth of field through wave-front coding. *Appl. Opt., AO* **34**, 1859–1866 (1995).

23 Jin, L. *et al.* Deep learning extended depth-of-field microscope for fast and slide-free histology. *Proceedings of the National Academy of Sciences* **117**, 33051–33060 (2020).

24 Seong, B. *et al.* E2E-BPF microscope: extended depth-of-field microscopy using learning-based implementation of binary phase filter and image deconvolution. *Light Sci Appl* **12**, 269 (2023).

25 Veening, J.-W., Smits, W. K. & Kuipers, O. P. Bistability, Epigenetics, and Bet-Hedging in Bacteria. *Annual Review of Microbiology* **62**, 193–210 (2008).

26 Bakshi, S. *et al.* Tracking bacterial lineages in complex and dynamic environments with applications for growth control and persistence. *Nat. Microbiol.* **6**, 783-791 (2021).

27 Tanouchi, Y. *et al.* A noisy linear map underlies oscillations in cell size and gene expression in bacteria. *Nature* **523**, 357-360 (2015).

28 Pengo, T., Munoz-Barrutia, A. & Ortiz-De-Solorzano, C. Halton sampling for autofocus. *J. Microsc.* **235**, 50-58 (2009).

29 Born, M. A. X. & Wolf, E. *Principles of Optics (Sixth Edition)* (Pergamon, 1980).

30 Coskun, A. & Oosterhuis, W. P. Statistical distributions commonly used in measurement uncertainty in laboratory medicine. *Biochemia Medica* **30** (2020).

31 Knapp, B. D. & Huang, K. C. The Effects of Temperature on Cellular Physiology. *Annu. Rev. Biophys.* **51**, 499-526 (2022).

32 Phadtare, S., Inouye, M. & Severinov, K. The nucleic acid melting activity of Escherichia coli CspE is critical for transcription antitermination and cold acclimation of cells. *J. Biol. Chem.* **277**, 7239-7245 (2002).

33 Horn, G., Hofweber, R., Kremer, W. & Kalbitzer, H. R. Structure and function of bacterial cold shock proteins. *Cell. Mol. Life Sci.* **64**, 1457-1470 (2007).

34 Friedman, H., Lu, P. & Rich, A. Temperature Control of Initiation of Protein Synthesis in Escherichi-Coli. *J. Mol. Biol.* **61**, 105-121 (1971).

35 Broeze, R. J., Solomon, C. J. & Pope, D. H. Effects of low temperature on in vivo and in vitro protein synthesis in Escherichia coli and Pseudomonas fluorescens. *J. Bacteriol.* **134**, 861-874 (1978).

36 Jones, P. G., Mitta, M., Kim, Y., Jiang, W. & Inouye, M. Cold shock induces a major ribosomal-associated protein that unwinds double-stranded RNA in Escherichia coli. *Proc. Natl. Acad. Sci. U.S.A.* **93**, 76-80 (1996).

37 Giuliodori, A. M., Brandi, A., Gualerzi, C. O. & Pon, C. L. Preferential translation of cold-shock mRNAs during cold adaptation. *RNA* **10**, 265-276 (2004).

38 Scott, M. & Hwa, T. Shaping bacterial gene expression by physiological and proteome allocation constraints. *Nat. Rev. Microbiol.* **21**, 327-342 (2023).

39 Scott, M., Gunderson, C. W., Mateescu, E. M., Zhang, Z. G. & Hwa, T. Interdependence of Cell Growth and Gene Expression: Origins and Consequences. *Science* **330**, 1099-1102 (2010).

40 Nordholt, N., van Heerden, J. H. & Bruggeman, F. J. Biphasic Cell-Size and Growth-Rate Homeostasis by Single Bacillus subtilis Cells. *Current Biology* **30**, 2238-2247.e5 (2020).

41 Kellogg, D. R. & Levin, P. A. Nutrient availability as an arbiter of cell size. *Trends in Cell Biology* **32**, 908–919 (2022).

42 Mueller, E. A., Westfall, C. S. & Levin, P. A. pH-dependent activation of cytokinesis modulates Escherichia coli cell size. *PLOS Genetics* **16**, e1008685 (2020).

43 Buda, R. *et al.* Dynamics of Escherichia coli's passive response to a sudden decrease in external osmolarity. *PNAS* **113**, E5838–E5846 (2016).

44 Ojkic, N., Serbanescu, D. & Banerjee, S. Antibiotic Resistance via Bacterial Cell Shape-Shifting. *mBio* **13**, e00659-22 (2022).

45 Amir, A. Cell Size Regulation in Bacteria. *Phys. Rev. Lett.* **112** (2014).

46 Wen, L. *et al.* Strong segregation promotes self-destructive cooperation. *ISME J* **19**, (2025).

47 Monod, J. The Growth of Bacterial Cultures. *Annu. Rev. Microbiol.* **3**, 371-394 (1949).

48 Klumpp, S., Zhang, Z. G. & Hwa, T. Growth Rate-Dependent Global Effects on Gene Expression in Bacteria. *Cell* **139**, 1366-1375 (2009).

49 Koch, A. L. Some Calculations on Turbidity of Mitochondria and Bacteria. *Biochim. Biophys. Acta* **51**, 429-441 (1961).

50 Ishimaru, A. *Wave propagation and scattering in random media* (Academic press New York, 1978).

51 Koch, A. L. Turbidity Measurements of Bacterial Cultures in Some Available Commercial Instruments. *Anal. Biochem.* **38**, 252-259 (1970).

52 Groen, F. C. A., Young, I. T. & Ligthart, G. A comparison of different focus functions for use in autofocus algorithms. *Cytometry* **6**, 81-91 (1985).

53 Geusebroek, J. M., Cornelissen, F., Smeulders, A. W. M. & Geerts, H. Robust autofocusing in microscopy. *Cytometry* **39**, 1-9 (2000).

54 Brandi, A., Spurio, R., Gualerzi, C. O. & Pon, C. L. Massive presence of the Escherichia coli 'majorcold-shock protein' CspA under non-stress conditions. *The EMBO Journal* **18**, 1653–1659 (1999).

55 Cavicchioli, R. *et al.* Scientists' warning to humanity: microorganisms and climate change. *Nat. Rev. Microbiol.* **17**, 569-586 (2019).

56 Zhu, M. L., Mu, H. Y. & Dai, X. F. Integrated control of bacterial growth and stress response by (p)ppGpp in Escherichia coli: A seesaw fashion. *Iscience* **27** (2024).

57 Wallden, M., Fange, D., Lundius, E. G., Baltekin, Ö. & Elf, J. The Synchronization of Replication and Division Cycles in Individual E. coli Cells. *Cell* **166**, 729-739 (2016).

58 Mahone, C. R. & Goley, E. D. Bacterial cell division at a glance. *J. Cell Sci.* **133** (2020).

## Methods

### Optical setup of LUNA-based platform

The optomechanical design was performed using CAD software (Dassault Systemes, SolidWorks). An infinity imaging system based on a commercialized microscope frame (Applied Scientific Instrumentation, RAMM) and a set of precision machined components was custom-built. The specimen was mounted on a motorized stage (MS2000) for planar motion. Axial movement of the objective was achieved by a motorized actuator with an encoder resolution of 5.5 nm (LS50). An anti-backlash routine was introduced at each small move to advantage for precision movement. Kohler illumination with a neutral white light source (Thorlabs, MNWHL4) was designed to provide brightfield and phase-contrast imaging mode. High-resolution images were collected using a sCMOS camera (PCO, Panda 4.2) with a 6.5 μm pixel size.

LUNA was installed in this imaging system. The light source was a fiber-coupled laser with a wavelength of 650 nm (output power < 5 mw), and was collimated to parallel beam by a fiber collimator. The wavelength was chosen to avoid crosstalk with the illumination for our bacteria imaging experiments and for a lower cost, although an infrared wavelength for more general applications could also be selected. An aspheric lens was inserted as the focal length extender (FLE), shifting the focal point of the laser beam to optimize the focusing range. The off-axis laser beam was introduced into the main optical train by a shortpass dichroic mirror (Semrock, FF625-SDi01). The diffraction pattern at the reflection plane was projected on a detector (Thorlabs, DCC1545M), whose pixel size is 5.2 μm. A cylindrical lens was placed before the detector to shape the diffraction pattern one-dimensionally to improve the detection accuracy. The full width at half maximum of the line projection of the crescent spot was approximately 30 μm wide, ensuring adequate subpixel accuracy. During the autofocusing procedure, a practical proportional-integral controller was used. The exposure time of the detector was set to 3~5 ms to avoid overexposure. Although LUNA was implemented on a bespoke imaging system, it is also compatible with other commercial

microscopes with infinity optics. Four objective lenses were tested for LUNA's performance (Table S1). Unless otherwise stated, data presented in the text was collected from the 100× oil objective.

The microfluidic chip was fixed into a custom-designed incubator, which adapts to the motorized stage. The incubator can be filled with distilled water in which the microfluidic chip is submerged to maximum heat conduction. Rubber rings are used in the design of the incubator to prevent water seepage. The sealable incubator has two pairs of fluidic conduits: fresh medium flows through the chip for cell growth by a pressure controller (FluidicLab, PC1); distilled water is circulated into the incubator for temperature change and maintenance. The culture temperature was maintained by the circulation of distilled water in an external thermostatic water bath driven by a peristaltic pump. The temperature of water inside the incubator was set to target during the experiments. In addition, the imaging objective was equipped with a lens heater.

**Numerical computations of the optical model**

Diffraction patterns near the focus of the optical system with circular aperture and coma aberrations can be handled by analyzing the wavefront distortion of an off-axis beam (Supplementary Note 2). The objective lens is treated as an ideal lens for the model demonstration. Consider an incident collimated Gaussian beam passing through the lens of radius $a$ and focal length $f$ (Figure S2a). According to the Huygens-Fresnel principle, the light disturbance at an arbitrary observation point $P$ in the vicinity of the focal point is determined by summing the contribution of each point $Q$ located where the incident Gaussian beam intersects the reference sphere on the pupil plane[29]. The coma aberration function can also be expressed in the polar coordinates ($\rho$, $\theta$) whose origin is the center of the pupil by $\Phi(\rho, \theta) = A_C\rho^3 \cos\theta$, where $A_C$ is the coefficient of primary coma[59]. The complex amplitude $U(P)$ is determined by calculating the diffraction integral over the intersection area $S$ on the reference sphere[29]:

$$U(P) = -\frac{\mathrm{i}k}{2\pi}\int\int_S U(Q)\frac{\exp(\mathrm{i}kq)}{q}\mathrm{d}S \tag{3}$$

where $k$ is the wavenumber, and $q$ is the distance between points $Q$ and $P$. For the incident beam with small off-axis amount involved, the inclination factor is approximated as unity and therefore is omitted in equation (3). The polar coordinates ($\rho$, $\theta$) are translated to ($r$, $\varphi$) with the origin of which ($\rho_0$, $\theta_0$) is situated at the beam center for convenience. The amplitude distribution of the Gaussian beam is given by $A_G \exp(-a^2r^2 / \omega^2)$, where $A_G$ is constant amplitude, and $\omega$ is beam waist. Furthermore, cylindrical coordinates ($u$, $v$, $\psi$) are introduced to specify an arbitrary point $P$ in the image field where $\psi$ is the azimuth at the focal plane ($x$, $y$), the dimensionless coordinates $v = ka\,(x^2 + y^2)^{1/2} / f = k\beta\,(x^2 + y^2)^{1/2}$ and $u = k\beta^2 z$. Then $U(P)$ is given by:

$$U(P) = -\frac{\mathrm{i}kA_G\beta^2}{2\pi}\int_0^{2\pi}\int_0^1 e^{-a^2r^2/\omega^2} e^{\mathrm{i}k\Phi_{TOTAL}(r,\varphi)}\, r\mathrm{d}r\mathrm{d}\varphi \tag{4}$$

The total phase term of $\Phi_{TOTAL}$ is defined by combining the like terms:

$$\begin{aligned} k\Phi_{TOTAL}(r,\varphi) &= k\Phi(r,\varphi) + k(q-f) \\ &= L_C + L_0(r) + L_1(r)\cos 2\varphi + L_2(r)\cos\varphi + L_3(r)\cos(\varphi-\psi) \end{aligned} \tag{5}$$

Define $\eta = (L_2^2 + L_3^2 + 2L_2L_3\cos\psi)^{1/2}$, $\tan\chi = -L_3\sin\psi / (L_2 + L_3\cos\psi)$. The integral difficulty of the intensity is simplified by expanding the exponential term $\exp(\mathrm{i}k\Phi_{TOTAL})$ with the help of the Jacobi-Anger identity and Graf's addition theorem, substituting the expended series in the integration, and integrating term-wise against $\varphi$. The intensity distribution of the diffraction pattern is developed in an infinite series:

$$I(u,v,\psi) = 4k^2{A_G}^2\beta^4\left|e^{\mathrm{i}L_C}\sum_{s=0}^{\infty}(-\mathrm{i})^s\int_0^1 e^{-a^2r^2/\omega^2}e^{\mathrm{i}L_0}J_s(L_1)J_{2s}(\eta)\cos(2s\cdot\chi)\,r\,\mathrm{d}r\right|^2 \tag{6}$$

where $J$ is a Bessel function of first kind. The term $s = 0$ is taken with the factor 1/2. Tedious calculation can be avoided because four terms in this expansion would suffice to keep the intensity variation within a few percent. The simplification greatly speeds up the numerical calculation of the intensity distribution. In the numerical computation, the selection of each parameter is as close to the actual optical path configuration as possible, such as $\beta = 1.25$ for the 100× objective lens, relative beam position ($\rho_0 = 0.1$, $\theta_0$

= 0°), and coma coefficient $A_C = 16\pi / k$. The coefficient $A_C$ is proportional to the tilt angle of the beam incident on the objective, and we have chosen a more representative value here.

**Ray tracing simulation of the model**

The optical design and numerical simulation of LUNA's optics were carried out based on ray tracing software (Zemax, OpticStudio), to validate LUNA's robustness under real-world optical limitations. A set of lenses was used to combine to substitute objective with an equivalent magnification of 100×. The other parameters of the optical elements were set exactly the same as the optical setup. For off-axis incidence, the normalized radial coordinate of the beam center at the objective rear aperture was specified to be approximately 0.15 (Figure S3b). To ensure full beam capture by the substitute lens system, the input beam size was reduced at the rear aperture via slight positional adjustment. A reflection surface was placed at the imaging space of the objective. Sequential intensity distributions on the reflection and detection plane were recorded as the reflection surface changes along the optical axis.

**Calibration of defocus dependence**

The measurement was carried out by scanning the objective from bottom to top along the optical axis around the focal plane. The reflected images on the detector were repeatedly recorded five times in repetitions at each step. The centroid coordinates of the light spot at sub-pixel precision were then computed from the captured images through basic morphological processing. The linear range was determined by finding the maximum $N$ multiples of DOF while maintaining the fitting root mean squared error (*RMSE*) less than 1 (Figure S6). The strict criteria for the linear range determination were selected to obtain high focusing sensitivity and accuracy near the focal plane.

Measurement repeatability is defined as the proportion of the total variation accounted for by the system variation to assess the system's measurement variation[60]. It indicates the degree of consistency during multiple measurements. The pooled standard deviation was used to calculate this variation underlying the monotonic response curve. A ratio below 10% is indicative of satisfactory system

612 performance[61]. All four test objectives demonstrate measurement repeatability of <2%, confirming the
613 robustness of the calibration relationship.

614 **Performance test of LUNA**

615 Timelapse tests with specific time intervals (1 second) were carried out and lasted for one hour for the
616 four objectives. Discrete drift thresholds varying from 5 nm to 50 nm at intervals of 5 nm were tested in
617 each condition. For the tests evaluating the focusing time, the time interval was altered. The objective and
618 sample temperature were maintained at 37 °C.

619 The extent of the perturbations can be reflected in the temporal fluctuations of spot intensity on the
620 same focal plane. This fluctuation may originate from laser instability, thermal effects in optical elements,
621 etc. The distribution parameters were extracted from the detector images. Random Gaussian noise
622 conforming to this distribution was generated and superimposed onto different spot images to simulate the
623 fluctuations, and the simulation was repeated 100 times on each image. Errors of the centroid locations
624 were employed to evaluate the impact of perturbations.

625 **Single-cell culture on microfluidic device**

626 A microfluidic chip was employed to track the long-term growth of bacteria, the structure of which
627 follows that of previously published: it consists of a series of microchannels perpendicular to the main
628 trench that perfuse the fresh medium[62]. The chip was fabricated based on soft lithography technique by
629 mixing dimethylsiloxane monomer and curing agent (Dow Corning, SYLGARD 184 Silicone Elastomer
630 Kit) in a ratio of 10:1, and then pouring into a mould, degassing and curing at 80 °C for one hour. The
631 PDMS chip was punched and bonded to a clean coverslip by air plasma treatment (Harrick Plasma, PDC-
632 002) for 30 seconds, followed by baking at 80 °C for five minutes.

633 *E. coli* K12 strains MC4100 and MG1655 were measured (MC4100 is presented in the text), in which
634 the flagella structural protein gene *fliC* and fimbriae structural protein gene *fimA* of MG1655 were knocked
635 out to prevent their escape from the microchannels. EZ rich defined medium (RDM) supplement with 0.4%

636 glucose was used[63]. The overnight culture grown from several colonies was subcultured twice and
637 centrifuged at a sufficiently high density. The concentrated culture was injected into the cleaned chip
638 passivated with bovine serum albumin, and the chip was spun to load cells into the microchannels. Fresh
639 medium was infused into the chip at a rate of 500 μL/hr by the pressure controller equipped with a 0.22
640 μm filter. Next, the incubator with the chip was sealed and placed on the motorized stage for time-lapse
641 imaging.

642 **Time-lapse imaging of bacterial under CS**

643 We developed a control software using MATLAB for the time-lapse imaging in the bespoke platform.
644 Users could set up imaging conditions and perform automation of experiments. The autofocusing control
645 is integrated, with the user only needing to set the desired plane as the focal plane. The output laser power
646 of LUNA at the objective front aperture was adjusted to ~5 μw, and the threshold was set as 50 nm.

647 Phase-contrast images were acquired with the 100× objective. Multiple microchannel sites (around 45
648 in each repeat experiment) were imaged every minute for 24-30 hours. Each image acquisition started right
649 after an autofocusing procedure. Approximately 1,100 single-cell data in total were collected in each repeat.
650 Cells were cultured at 37 °C to steady-state for about four hours before CS. By mixing ice into the external
651 water bath, the incubator temperature can be downshifted to 14 °C within 5 minutes and maintained until
652 the end of the time-lapse experiment. Although the exact temperature around bacterial cells in the
653 microfluidic chip could not be directly measured, the high thermal conductivity at the water-glass interface
654 ensures rapid thermal equilibration. When the temperature was lowered, the objective lens heater was
655 stopped, which caused a slightly longer focusing time. At least 3 repeated experiments were carried out for
656 each of the two strains.

657 **Image analysis and data process**

658 Hundreds of cells at the bottom of microchannels were imaged sequentially. We developed a custom
659 algorithm routine to analyze phase-contrast images using MATLAB: Microfluidic Architecture based
660 Resilient Contour Expansion Analysis (MARCEA) (Figure S11a). Raw images were denoised and

661 segmented to identify individual cells. The contours of the segmented cells were iteratively adjusted based
662 on a rod-shaped model to adapt to the deformation of the cells, thereby extracting their accurate spatial
663 features. Microchannels were automatically aligned for cell tracking (Figure S11b). A cell division event
664 was determined according to the large drop of the width and intensity at the split position. Using the
665 processing routine, complete analysis of ~65,000 images costs ~80 mins for each experiment on a standard
666 computer with ten physical cores.

667 A total of 10,040 cell cycles from 784 lineages were used to statistically analyze their behaviors.
668 Outliers within each cell cycle were ignored when calculating those time-dependent properties including
669 sizes and elongation rates. Aberrant cell cycles such as filamentation were excluded from each experiment.
670 Groupings of cell lineages according to their relative moments (values from 0 to 1) of CS onset within G0
671 lifespan were employed. Groupings are centered at intervals of 0.1, and each group encompasses a range
672 of ± 0.05 around the center value.

673 **The allocation of protein synthesis during CS**

674 The allocation of protein synthesis is extracted from the published protein abundance data[5]. In brief,
675 a certain protein's abundance equals its length multiplied by its number at sampling time. And total protein
676 abundance is the sum of them. The allocation of protein synthesis to given proteins is calculated as the ratio
677 of the change in their abundance to the change in total protein abundance between consecutive time points.
678 Specifically, for 37 °C condition, protein synthesis allocation is directly equal to the corresponding protein
679 abundance. This analysis focuses on the ribosome and CSPs. Ribosome allocation is derived from the sum
680 of allocations to its constituent ribosomal subunits. And the CSPs include the most highly induced 45 genes
681 after CS[5]. Filtered genes in the original paper are not included. Although the duration of acclimation varies
682 with temperature (~2 h at 14 °C, ~4 h at 12 °C, and ~6 h at 10 °C), the corresponding increases in total
683 protein synthesis are comparable (13% at 12 °C in this study; 12% at 10 °C from Ref. 15). To ensure
684 consistent comparison across temperatures, we selected three standardized time points to illustrate: before
685 CS (37 °C), mid-acclimation (3 h), and the end of acclimation (6 h).

686 **Experiments of batch culture**

687 Both *E. coli* MC4100 and MG1655 strains were measured (MC4100 is presented in the text unless
688 otherwise stated). A few single colonies from a Luria-Bertani agar plate were picked. Cells were cultured
689 overnight at 37 °C in RDM and then placed in a thermostatic shaking water bath at 37 °C after subculture
690 three times (> 10 mass doublings). The bacterial population was proven to reach a steady-state by then[63].
691 The measurements started when the cells were diluted again to an OD of 0.02 at 600 nm, with a sampling
692 interval of 15-30 minutes. The $OD_{600}$ value was determined using a spectrophotometer (Thermo Fisher
693 Scientific, Genesys 150), with an average of three readings taken. 50 μl of the cell suspension was taken
694 and fixed with the 450 μl of precooled fixation buffer (0.12% formaldehyde with 0.9% NaCl, filtered with
695 a 0.22 μm filter), then used to measure the cell concentration and volume through a flow cytometer
696 (Beckman Coulter, CytoFLEX S) in three parallel samples (Supplementary Note 5). Average cell volume
697 was determined by the median of the forward scatter signals (FSC-A). A variant method called axial light
698 loss detection is employed on the cytometer to detect FSC intensity, which is directly proportional to the
699 cell volume regardless of the refractive index and thus benefits[64]. Further quantitative research also
700 supports the relationship[63]. For the experiments with CS, when $OD_{600}$ reached about 0.2, the culture
701 temperature was gradually lowered to 14 °C or 12 °C within five minutes by mixing ice into the water bath.

702 **Total protein quantification**

703 Total protein quantification was carried out according to previous studies using the Biuret method[65,66].
704 We quantified changes in total protein to represent $\Delta M$ since $M$ is roughly proportional to the protein
705 amount[67]. The MG1655 strain was selected and followed the culture procedure. The temperature was
706 lowered to 12 °C to ensure a sufficiently long acclimation (~5 hours) and higher resolution. Two sampling
707 time points were at the beginning and near the end of the acclimation, respectively. Cell cultures were
708 collected by centrifugation in triplicate (4 ml each) at each time point. The cell pellet was rinsed with 1 ml
709 0.9% NaCl solution, re-suspended in 0.2 ml water, and snap frozen in liquid nitrogen. The cell pellet was
710 then thawed in a room temperature (RT) water bath. To extract proteins, 0.1 ml 3M NaOH was added,

incubated at 100 °C heat block for 5 min, and cooled in water bath at RT for 5 min. Then 0.1 ml 1.6% $CuSO_4$ was added to the sample, shaken and mixed thoroughly, and allowed to stand for 5 min. The sample was centrifuged and OD value at 555 nm was read by the spectrophotometer. The protein amount of the sample was determined from the standard curve of bovine serum albumin obtained on the day of the experiment using the same procedure.

**Simulation with the Rayleigh-Gans approximation**

The intraparticle interference can be corrected by introducing a form function $P(\theta)$ to the Rayleigh differential scattering cross section $\sigma_d$. If the relative refractive index of the scatterer in the surrounding medium ($m = n_s / n_m$) approaches to 1, $\sigma_d$ can be simplified as:

$$\sigma_d = \frac{\mathrm{d}\sigma}{\mathrm{d}\Omega} = \frac{k'^4 V^2}{8\pi^2}(m-1)^2(1+\cos^2\theta)P(\theta) \tag{7}$$

where $k'$ is the wavenumber in the medium, $V$ is scatterer's volume, and $\theta$ is angle of observation. The refractive indices of *E. coli* and the surrounding medium are estimated as 1.384 and 1.338 at illumination wavelength of 600 nm[68], respectively, thus meeting the prerequisites of the above equation. Furthermore, the refractive index difference between the scatterer and the medium is proportional to the dry-mass density $\rho_{dry}$, with a scaling factor of the specific refraction index increment[68-70], hence the quantity ($m$ – 1) can be substituted by $\rho_{dry}$. The $P(\theta)$ for differently shaped scatterers have different analytical forms. Ellipsoid of revolution as the form function is adopted to describe single *E. coli* cell, which has the following form:

$$P = \left[\frac{3}{x^3}(\sin x - x\cos x)\right]^2, x = k'w\sin\frac{\theta}{2}\sqrt{\sin^2\beta + \gamma^2\cos^2\beta} \tag{8}$$

where $\beta$ is the orientation angle between the ellipsoid and the direction bisecting the incident and the scattered light beam, $w$ is width, and $\gamma$ is aspect ratio. For randomly oriented bacteria in the medium, the form function should be averaged over all equally probable orientation angle $\beta$. Over a thousand cells with appropriate parameter ranges, were simulated to compute the total scattering cross section $\sigma$ by integrating $\sigma_d$ over all angles except the detecting regime. Equivalent volume and aspect ratio were chosen as two independent determining parameters (ranging from 0.5 ~ 5 $\mu m^3$ and 2.5 ~ 5, respectively) to simulate cells.

To account for the uncertainty in the detection angle, we combined a series of integrals with lower bounds on $\theta$ varying from 0.5° to 3° at 0.5° interval and upper bounds of 180°.

## Data availability

All the data used in this study are available upon reasonable request to the corresponding author.

## Code availability

All codes are available upon reasonable request to the corresponding author for nonprofit academic research use only. Codes for controlling the LUNA-enabled bespoke platform and analyzing raw images are available in executable forms.

## References


59 Yoshida, A. & Asakura, T. Diffraction Patterns of Off-Axis Gaussian Beams in Optical System with Astigmatism and Coma. *Opt. Commun.* **25**, 133-136 (1978).

60 Nakagawa, S. & Schielzeth, H. Repeatability for Gaussian and non-Gaussian data: a practical guide for biologists. *Biol. Rev.* **85**, 935-956 (2010).

61 Chrysler Corporation, F. M. C., General Motors Corporation. *Measurement Systems Analysis (MSA)* (AIAG, 2010).

62 Wang, P. *et al.* Robust Growth of Escherichia coli. *Curr. Biol.* **20**, 1099-1103 (2010).

63 Zheng, H. *et al.* General quantitative relations linking cell growth and the cell cycle in. *Nat. Microbiol.* **5**, 995-1001 (2020).

64 Brittain, G. I. V. *et al.* A Novel Semiconductor-Based Flow Cytometer with Enhanced Light-Scatter Sensitivity for the Analysis of Biological Nanoparticles. *Sci. Rep.* **9** (2019).

65 You, C. H. *et al.* Coordination of bacterial proteome with metabolism by cyclic AMP signalling. *Nature* **500**, 301-306 (2013).

66 Herbert, D., Phipps, P. & Strange, R. *Methods in microbiology* (Elsevier, 1971).

67 Basan, M. *et al.* Inflating bacterial cells by increased protein synthesis. *Mol. Syst. Biol.* **11** (2015).

68 Oldewurtel, E. R., Kitahara, Y. & van Teeffelen, S. Robust surface-to-mass coupling and turgor-dependent cell width determine bacterial dry-mass density. *Proc. Natl. Acad. Sci. U.S.A.* **118** (2021).

69 Barer, R. Interference Microscopy and Mass Determination. *Nature* **169**, 366-367 (1952).

70 Koch, A. L., Robertson, B. R. & Button, D. K. Deduction of the cell volume and mass from forward scatter intensity of bacteria analyzed by flow cytometry. *J. Microbiol. Methods* **27**, 49-61 (1996).

**Acknowledgements**

We thank H. Cao for providing MG1655 strain. We thank H. Zheng for discussions. This work was supported by the National Key R&D Program of China (Grant No. 2020YFA0908800), Strategic Priority Research Program of the Chinese Academy of Sciences (Grant No. XDB0480000), National Natural Science Foundation of China (Grant No. 32071417).

**Author contributions**

S.L. devised LUNA, developed the optical model and numerical simulation, performed the implementation and evaluation of LUNA, devised and implemented the LUNA-enabled bespoke platform, developed the standalone control software, developed image processing algorithm MARCEA, developed the scattering model and performed simulations on OD measurements, and analyzed all the experiments data. Z.M. participated in the evaluation of LUNA, conceived the biological experiments, prepared the bacteria samples, performed the biological experiments, and participated in the biological data analysis. Y.Y. designed the microfluidic chip, conceived the biological experiments, and participated in the biological data analysis. J.W. and Y.S. prepared the bacteria samples and performed the biological experiments. X.C. participated in the discussion of optical principle and the evaluation of LUNA. X.F. participated in the discussion of biological experiments. S.H. conceived the whole project and supervised the research. S.L. wrote the paper with contributions from all of the authors.

**Competing interests**

The authors declare no competing interests.

**Supplementary Information** is available for this paper.

**Correspondence and requests for materials** should be addressed to Shuqiang HUANG.